경사 전극 배열을 이용한 고밀도 하드 디스크의 마이크로 구동부 제작

최 석 문[1)] · 박 성 준[*2)]

삼성전기 중앙연구소[1)] · 충주대학교 기계공학과[*,2)]

A Microcatuator for High-Density Hard Disk Drive Using Skewed Electrode Arrays

Seok-Moon Choi[1)] · Sung-Jun Park[2)]

1)R&D Center, Samsung Electro-Mechanics, Suwon, Korea
2)Department of Mechanical Engineering, Chungju National University, Chungju, Korea

Abstract : This paper reports the design and fabrication of a micro-electro-mechanical-system(MEMS)-based electrostatic angular microactuator for a dual-stage servo. The proposed actuator employs a novel electrode pattern named "skewed electrode array(SEA)" scheme. It is shown that SEA has better linearity than a parallel plate type actuator and stronger force than a comb-drive based actuator. The moving and the fixed electrodes are arranged to make the driving force perpendicular to the rotating moment of arm. By changing the electrode overlap length, the magnitude of electrostatic force and stable displacement will be changed. In order to optimize the design, an electrostatic FE analysis was carried out and an empirical force model was established for SEA. A new assembly method which will allow the active electrodes to be located beneath the slider was developed. The active electrodes are connected by inner and outer rings lifted on the base substrate, and the inner and outer rings are connected to platform on which the slider locates. Electrostatic force between active electrodes and platform can be used for exiting out of plane modes, so this provides the possibility of the flying height control. A microactuator that can position the pico-slider over ±0.5μm using under 20 volts for a 2 kHz fine-tracking servo was designed and fabricated using SoG process.

Key words : Skewed Electrode Array (경사 전극 배열), Microactuator (미소구동부), Hard Disk Drive (하드디스크)

1. Introduction

The areal density of a magnetic hard disk drive (HDD) is the product of the linear bit density, which is the number of data bits written along the circumferential direction of a data track, and the track density, which is the number of data tracks per radial length in the disk. Currently, areal density is growing at a rate around 60% per year and linear bit density is

10-20 times greater than track density. So, it would be expected that the acceleration in the rate of increases in track density will need to keep the growing rate because of the deceleration in the linear bit density. Track density mainly depends on the performance of track-following servo system. But there are many disturbances that limits the performance of the track following servo such as resonance of head-gimbal assembly (HGA), or non-linearity of pivot bearing in voice coil motor (VCM)[1]. A dual-stage servo system, which uses a VCM as a coarse, low-bandwidth

[*] Corresponding author. E-mail: park@cjnu.ac.kr

actuator, and a microactuator as a fine, high band-width actuator, was thus devised to improve the track following [2].

There are three types of actuation principles in dual-stage actuation. The first is a suspension moving type which places piezoelectric actuator at steel suspension [3-7]. The second is a head moving type in which the actuator is located on a slider and directly moves the read/write head [8-10]. The third is a slider moving type. In this type, the microactuator is placed between the slider and the gimbal of a conventional suspension as shown in Fig. 1[11-16]. An angular actuation scheme was adopted. It has a high lateral stiffness and is insensitive to external shock and vibration. Resonant frequencies such as in plane and out of plane modes can be tuned by selecting the geometrical parameters of flexural suspension. For area efficient design, active electrodes are arranged under slider by connecting moving electrodes and inner and outer rings lifted on the base substrate and polysilicon layer acts as mechanical anchor and electrical contact is located beneath the active electrodes. Also, efficient angular actuation is achieved by putting the more electrodes in outer region. Active electrodes are located beneath the slider by forming the platform which connects the slider with the microactuator. Electrostatic force between active electrodes and platform can be used for exiting out of plane modes.
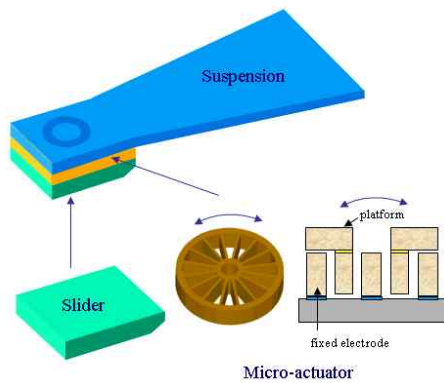
2. Electrostatic Actuation Scheme
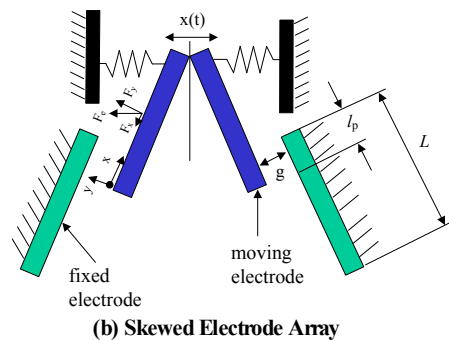
2.1 Skewed Electrodes Array

Skewed Electrodes Array for angular actuation scheme is shown in figure 2. The moving and the fixed electrodes are arranged to make the driving force perpendicular to the rotating moment of arm. The electrostatic force between the moving and fixed electrode, F_e, can be divided into two force components, F_x and F_y. By changing the electrode overlap length, l_p, the electrostatic force and the angle ϕ will be changed.

$$F_e = \sqrt{(F_x^2 + F_y^2)} \qquad (1)$$

$$\phi = \tan^{-1}(F_x/F_y)$$
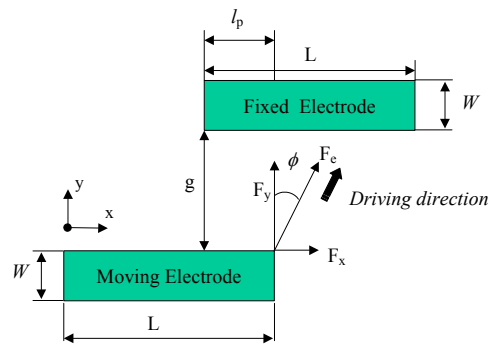
(a) Analysis model

(b) Skewed Electrode Array

Fig. 2 Electrode configuration and analysis model of SEA

Fig. 1 Dual stage micro-actuator

2.2 Approximation of electrostatic force model

Generally, the ratio of overlap electrode length to width, l_p/W, in commonly used electrostatic actuators such as comb-drive, parallel plate is large enough to neglect fringing field effects. In the SEA, where the ratio of l_p/W is less than 5, the fringe field plays start affecting the electrostatic forces, F_x and the F_y. It is very difficult to calculate electrostatic force Fe including fringe field effect analytically. In order to estimate this effect, electrostatic force Fe can be decomposed into force components F_x and F_y. AFE analysis was carried out for the model in figure 2 (b) with the following condition: driving voltage = 10V, $L_s = L_m$, $W_s = W_m$

Figure 3 shows the calculated electrostatic force component F_x per unit height. The comb-drive force per unit height neglecting fringe field effect was determined using equation (4). Due to the influence of fringe field, the force F_x component on the SEA model was slightly lower than comb-drive force less than $l_p/L = 0.5$ and the difference increases with increasing l_p/L. As shown in figure 3, F_x can be determined as follows for less than $l_p/L = 0.5$.

$$F_x = \alpha \times (\frac{1}{2} \frac{\varepsilon_a h}{g} V^2) \tag{2}$$

where, ε_a is the permittivity of air, g is the gap between moving and fixed electrode, V is the input voltage and is the correction factor of F_x considering the fringe field effect.
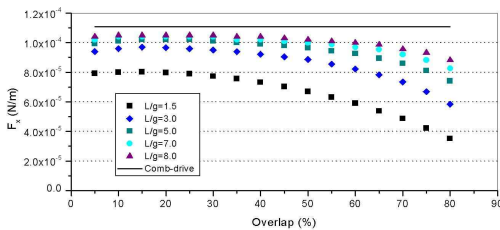

Fig. 3 F$_x$ according to overlap

In order to determine the correction factor alpha, alpha-gap characteristics of SEA are calculated as illustrated in Figure 4. Assuming linear decrease of the correction factor, α, with the gap, g, the correction factor can be denoted as:

$$\alpha = (A \times g) + 1 \tag{3}$$
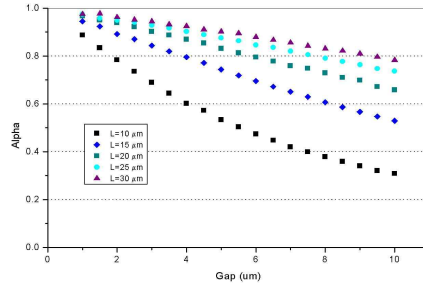
where, A is a function of the electrode length L.

Fig. 4 F$_x$ correction factor according to gap

For determination the slope of correction factor α, α-L characteristics have been calculated. As illustrated in figure 5, 3-rd order polynomial curve fitted line shows good agreement with FEM results.

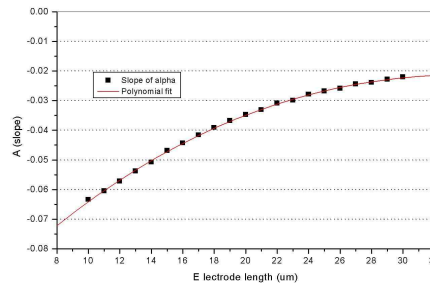$$A = c_1 L^3 + c_2 L^2 + c_3 L + c_4 \tag{4}$$

Fig. 5 Slope of alpha according to electrode length

The contribution of the fringe field effect to the force component F_y was investigated for the SEA model. Figure 6 shows the calculated electrostatic forces F_y per unit height of FE models and parallel plate. Due to the influence of the fringe field, the force F_y on the SEA model was higher than parallel plate force. As

illustrated in figure 6, the force difference between parallel plate model and FEM is constant with increasing overlap length. Therefore, F_y can be expressed as the following equation:

$$F_y = \frac{1}{2} \frac{\varepsilon_a l_p}{g^2} V^2 + \beta V^2 \qquad (5)$$

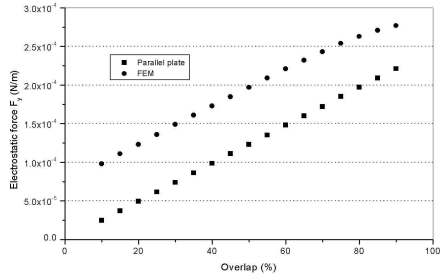where, β is the correction factor of F_y for fringe field which depends on the electrode configuration.

Fig. 6 F_y according to overlap

To obtain the influence of fringe field effect on F_y, β -gap characteristics at various electrode length and width are investigated. As shown in figure 7, beta decreases with the gap and for a given gap the value of beta is constant at various electrode length and width. Consequently, β can be denoted as the following equation:

$$\beta = \frac{B}{g}, \ g > 0 \qquad (6)$$

where, B is the curve fitted value by considering gap and driving displacement.
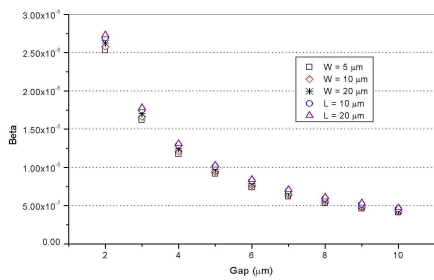

Fig. 7 Beta according to gap

2.3 Evaluation of the approximative force model

A simulation was performed to compare between the approximative model and the FE model of the SEA in figure 2. The specification of the geometry used for calculation is shown in Table 1. For a given design specification, the electrostatic force components in each direction can be determined.

$$F_x = (Ag+1) \times \left(\frac{1}{2} \frac{\varepsilon_a}{g} V^2 \right), \qquad (12)$$

$$A = (1.18E-6)L^3 - (1.42E-4)L^2 + (6.17E-3)L - 1.12$$

$$F_y = \frac{1}{2} \frac{\varepsilon_a l_p}{g^2} V^2 + \frac{4.12E-12}{g} V^2 \qquad (13)$$

Table 1 Electrodes specification of SEA

Parameters	Symbol	Value
Length of stationary electrode	L_s	20 μm
Length of moving electrode	L_m	20 μm
Width of stationary electrode	W_s	20 μm
Width of moving electrodes	W_m	6 μm
Initial gap between electrodes	g	6 μm
Overlap length	l_p	6 μm
Driving voltage	V	18 volt

Electrostatic forces of conventional actuators and the SEA can be compared as shown in figure 8. Same geometrical conditions were applied for each actuator. The simulation result shows that the proposed SEA can generate almost 2 times of force generated by the comb-drive for $0.1 < l_p / L$.
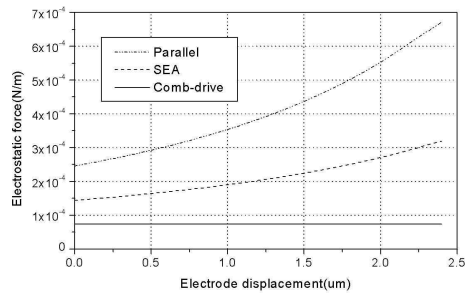

Fig. 8 Electrostatic force of actuation schemes

Figure 9 shows the calculated driving force with moving electrode displacement when the overlap length varies from 10% to 50%. The moving electrode moves to the intersection of an electrostatic driving force curve and the straight line where electrostatic force and spring force cross. Intersection of the spring force and the electrostatic force indicates equilibrium position. Above this point pull-in instability which the moving electrode comes into contact with the fixed electrode occurs and the actuator is unstable. Thus, under this equilibrium condition, the moving electrode can only one-third of the initial gap in parallel plate actuation [2]. In SEA, the stable stroke can be varied by changing the overlap electrode length. The selection of overlap electrode length has opposite effect on stable stroke and driving force. For decreasing the overlap length, the stable stroke becomes large in SEA. Consequently, the greater the overlap length is, the smaller stable stroke and the larger driving force become, as shown in figure 9. Simulation results show that the proposed SEA generates the stable displacement 20-40 % grater than the parallel plate for $0.1 < l_p/L < 0.5$.
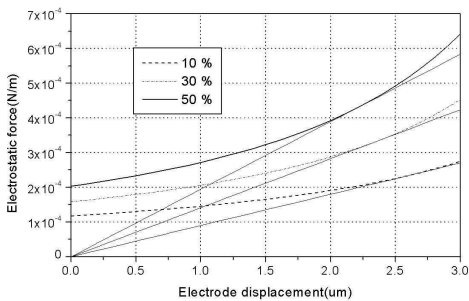

Fig. 9 Electrostatic force at various overlap electrode length

3. Design of Angular Microactuator for HDD

3.1 Design

The angular electrostatic microactuator using skewed electrode array (SEA) scheme was designed. Figure 10 (a) illustrates electrodes arrangement of SEA unit. Each unit of SEA is arranged up to 1mm radius. Figure 10 (b) illustrates electrodes arrangement for

angular actuation. Electrode interval, which is the distance between each electrode pair, is determined by considering the interaction of neighboring electrodes. The moving electrodes are connected by inner and outer rings lifted on the base substrate, and the inner ring is connected to the flexural suspensions that are anchored to the rotating center. The specifications of angular microactuator are defined in Table 2.
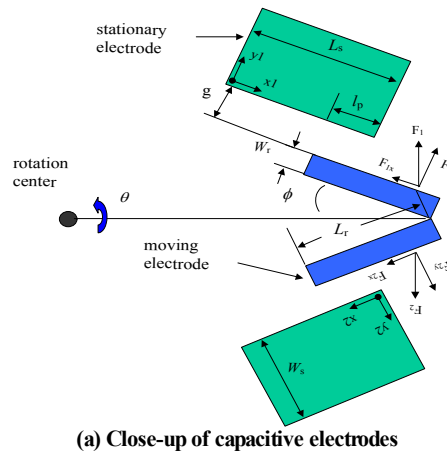
(a) Close-up of capacitive electrodes
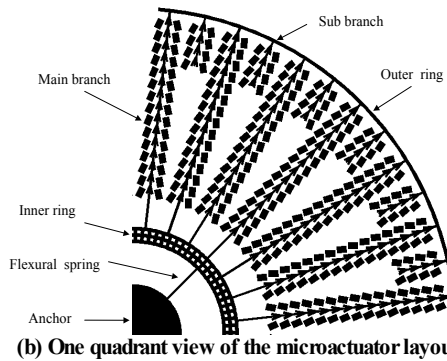
(b) One quadrant view of the microactuator layout

Fig. 10 Electrodes arrangement of SEA

Electrostatic actuators are square law device. A typical approach to linearizing the output force is differential driving which gives Vb+Vc and Vb-Vc to upper and lower fixed electrode respectively. Using this differential drives and assuming overlap length lp constant during the rotation, the total electrostatic force

Table 2 Design parameters of angular microactuator

Parameters	Design 1 ($l_p=2\mu m$)	Design 2 ($l_p=6\mu m$)	Design 3 ($l_p=10\mu m$)
No. of main branch	24	24	24
No. of sub branch	21	21	21
No. of cell in main branch	21	21	21
No. of cell in sub branch	5	6	6
Distance between unit cells	29 μm	27 μm	26 μm
Skew angle	28.7°	19.9°	13.9°
Overlap electrode length	2 μm	6 μm	10 μm
Radius of starting unit cell in main branch	473 μm	453 μm	453 μm
Radius of starting unit cell in sub branch	865 μm	861 μm	861 μm

is the difference between the force contributed by the left stationary electrode and right stationary electrode.

$$F_{e,unit} = F_1 - F_2 = K_{e,unit}\theta + K_{v,unit}V_c \qquad (9)$$

where,

$$K_{e,unit} = lV_b^2\left[2\cos\phi\left(\frac{\varepsilon_a l_p}{g^3} + \frac{B}{g^2}\right) + \sin\phi\left(\frac{\varepsilon_a}{g^2}\right)\right]$$

$$K_{v,unit} = 2V_b\left[\cos\phi\left(\frac{\varepsilon_a l_p}{g^2} + \frac{2B}{g}\right) + \sin\phi\left(\varepsilon_a A + \frac{\varepsilon_a}{g^2}\right)\right]$$

Consequently, the driving torque is the sum of the unit cell torque

$$T(V_b, V_c, \theta) = \sum_{i=1}^{n} T_{unit} = \sum_{i=1}^{n} l_i F_{e,unit} = K_e\theta + K_v V_c \quad (10)$$

where, n is the total number of SEA unit and l_i is the length of moment arm at each SEA unit.

3.2 Dynamics of a microactuator

There are two requirements in designing a dual stage actuator of a hard disk drive; the actuator should be insensitive to external shocks and vibrations and should not influence the slider dynamics. To meet these requirements, the mass moment of inertia of the microactuator should be minimized. And the resonant frequency must be tunable by selecting design parameters. To reduce the moment of inertia of the

microactuator, we designed diameter of the microactuator to be 2 mm which is slightly larger than conventional pico-slider. In order to allow the microactuator to be controlled, the resonant frequencies for tracking mode (along the data track) must be either well below or well above the tracking servo bandwidth. Increasing resonant frequency of tracking mode reduces the microactuator displacement, so choosing a resonant frequency below tracking servo bandwidth is efficient. To achieve a bandwidth of 2 kHz, resonant frequencies of tracking and pitch modes were tuned to be 1400 Hz, 9100 Hz, respectively. Using the design parameters in Table 3, width of flexural suspension is 4 μm with the following data: anchor radius is 130 μm, length of flexural suspension is 170 μm, and number of flexural suspension is 4.

Table 3 Microactuator design parameters

Parameters	Symbol	Value
Moment of inertia of pico-slider	l_s	3.61E-13 kgm^3
Moment of inertia of microactuator	l_m	2.54E-13 kgm^3
Gap between moving and fixed electrode	g	6 μm
Overlap length of moving and fixed electrode	l_p	10 μm
Height of electrode	h	100 μm
Nominal bias voltage	V_b	12 volt
Control voltage	V_c	8 volt
Mechanical stiffness of flexural spring	K_m	4.81E-5 Nm/rad
Electrostatic stiffness	K_e	1.59E-5 Nm/rad

A modal analysis was performed to investigate the microactuator dynamics with a pico-slider using ANSYS. Track following and pitch mode with pico-slider is shown in figure 11. Figure 12 shows the microactuator rotation with the control voltage, Vb=12 V. In order to move the pico-slider to 0.5 μm, rotation angle of microactuator is to be 0.8 mrad, thus overlap electrode length is 10 μm under driving voltage restraint. Driving torque with Vb=12, Vc=8 is shown in figure 13. The slope of driving torque (solid line) is electrostatic stiffness. Mechanical restoring torque is shown as dotted line.
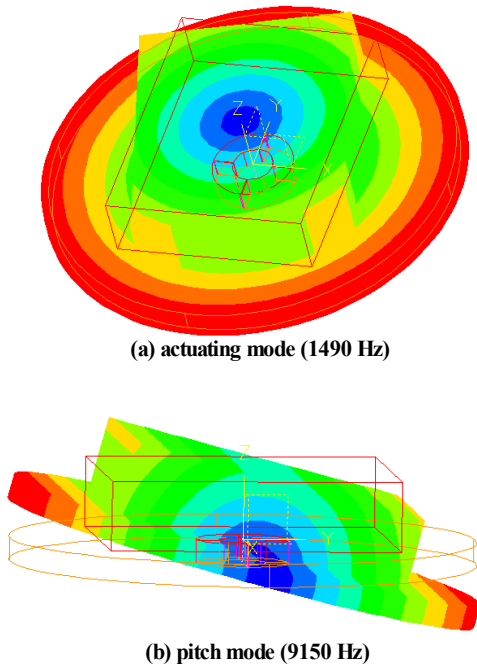
(a) actuating mode (1490 Hz)

(b) pitch mode (9150 Hz)

Fig. 11 Modal analysis of microactuator with picoslider

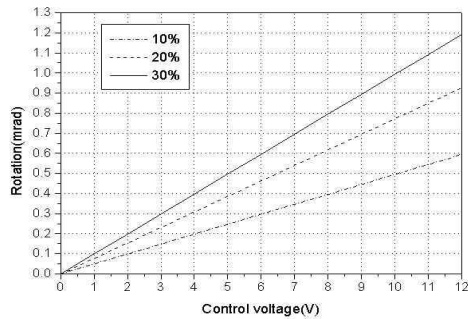**Fig. 12 Rotation angle of microactuator with pico-slider according to control voltage : Vb=12 V**
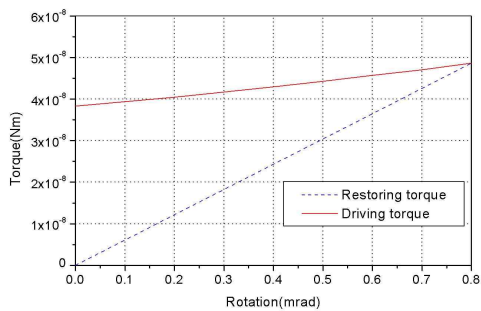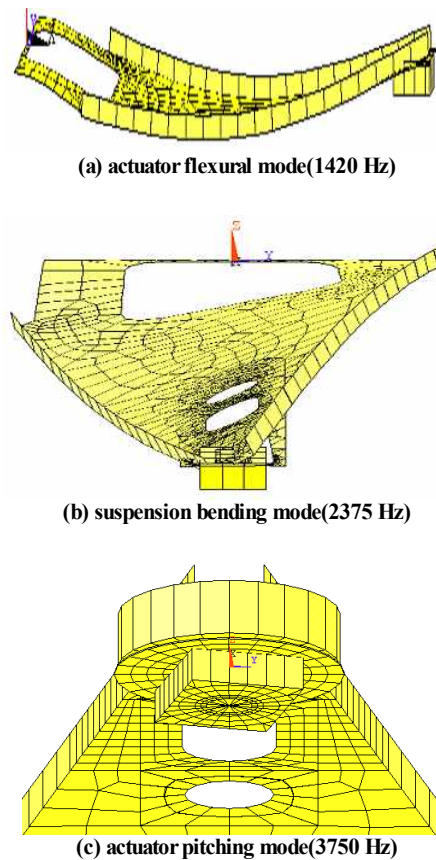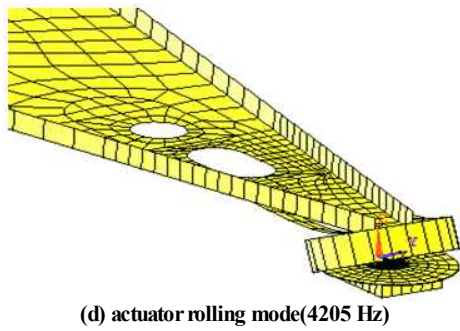

Fig. 13 Driving torque according to rotation

3.3 Dynamics of a dual-stage HGA

Modal analysis under loading conditions was conducted to investigate the microactuator dynamics with a pico-slider and type 2030 suspension (Hutchinson). Resonant frequencies and mode shapes of in plane and out of plane are listed in Table 2. The steel suspension bending modes that can be found in single HGA and dual-stage HGA are not affected by an added mass of the microactuator. The pitch and roll modes of the microactuator show in Fig. 14 of a dual-stage HGA are above 4 kHz. It is suitable for a high-bandwidth (above 2 kHz) servo. The sway mode which originated from gimbal stiffness is very important because it directly effects on tracking accuracy. The sway mode slightly changed after placing the microactuator. So, it can be found that the microactuator does not interfere the slider dynamics.

(a) actuator flexural mode(1420 Hz)

(b) suspension bending mode(2375 Hz)

(c) actuator pitching mode(3750 Hz)

(d) actuator rolling mode(4205 Hz)

Fig. 14 Modal analysis of HGA microactuator with in loading condition

Table 4 Comparison conventional SHGA with dual-stage HGA

Single-stage HGA		Dual-stage HGA	
Mode	Frequency	Mode	Frequency
1st suspension bending	2013 Hz	Actuating mode	1490 Hz
1st suspension torsion	2868 Hz	1st suspension bending	2374 Hz
2nd suspension bending	6260 Hz	1st suspension torsion	3022 Hz
2nd suspension torsion	8409 Hz	Actuator rolling	3750 Hz
Sway	12550 Hz	Actuator pitching	4205 Hz
Membrane	12991 Hz	2nd suspension bending	161 Hz
3rd suspension torsion	14303 Hz	2nd suspension torsion	9025 Hz
4th suspension torsion	17306 Hz	Sway	11073 Hz
		membrane	12788 Hz

4. Fabrication process

The fabrication process for the angular microactuators is presented in figure 15. First, oxide layer is deposited as a sacrificial layer by PECVD. After first photolithography, oxide layer is patterned to form mechanical anchor and electrical contacts (a). The polysilicon deposited by LPCVD. After second photolithography, polysilicon is selectively doped to

achieve electrical contact and insulation (b). CMP is used for planarization of polysilicon layer to bond with glass wafer. The polysilicon layer over the Si-structure is bonded with glass that acts as a base substrate(c). Subsequently, the silicon is patterned and a high aspect ratio microstructure is achieved by ICP-RIE (d). Then the platform is aligned to bond with the moving electrodes. Finally, the sacrificial layer is chemically etched away using HF and the structure is released (e).


(a) Oxide deposition and patterning

(b) Polysilicon deposition and doping

(c) Anodic bonding and Si thinning

(d) ICP-RIE

(e) Platform bonding and release
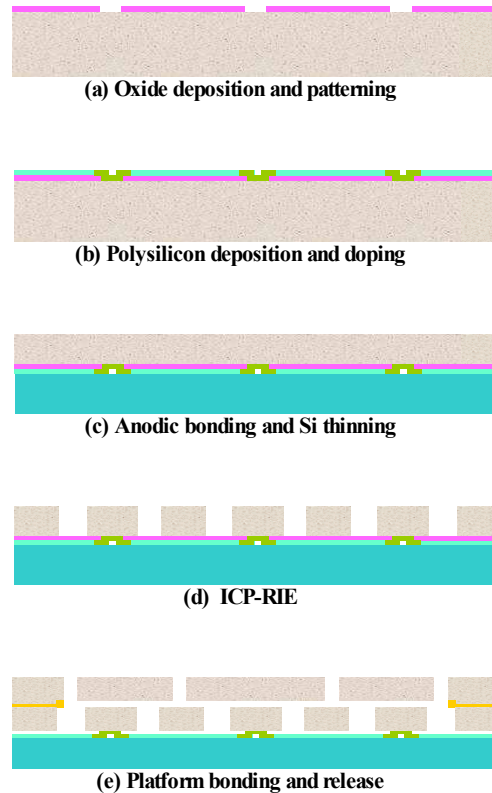
Fig. 15 Fabrication process

Figure 16 shows the SEM photographs of microactuator. The moving electrodes are connected by inner and outer rings lifted on the base substrate, and the inner ring is connected to flexural suspensions that are anchored to the rotating center. For efficient angular actuation, the more active electrodes are arranged in outer region increasing the driving moment.
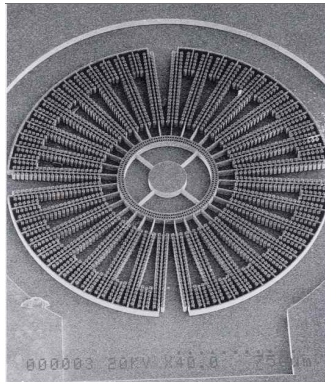
(a) microactuator without platform
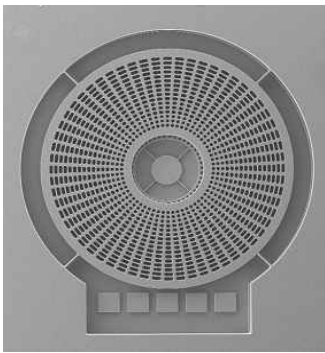
(b) microactuator with platform

Fig. 16 SEM photographs of microactuator

Fig. 17 SEM photograph of the microactuator with pico-slider

Fig. 18 FRF of the microactuator with pico-slider : rotation
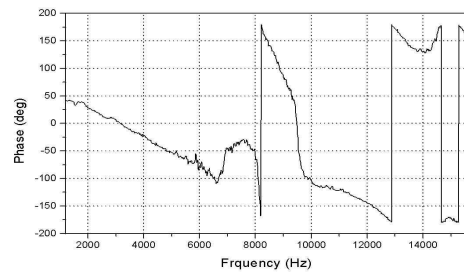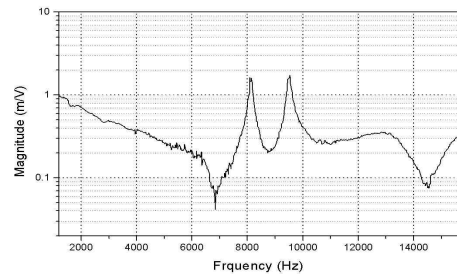
Fig. 19 FRF of microactuator with pico-slider : pitch & roll

5. Results

Measurement of the microactuator frequency response was performed using laser doppler vibrometer(LDV). Figure 17 shows the microactuator assembled pico-slider. The measured frequency response function, both tracking and pitch direction, is shown in figure 18-19. Note that measured resonant frequency is slightly deviated from the designed. Actually, the microactuator height was slightly reduced during CMP process. This difference results in reduction of flexural suspension stiffness. And, the beam width of flexural suspension was slightly narrower than designed, resulting in additional reduction of suspension stiffness.
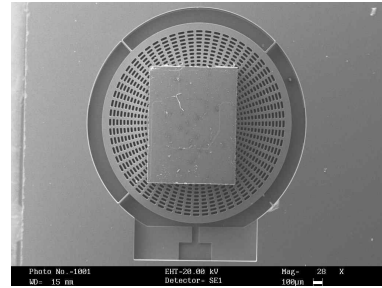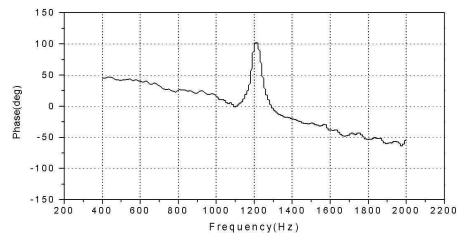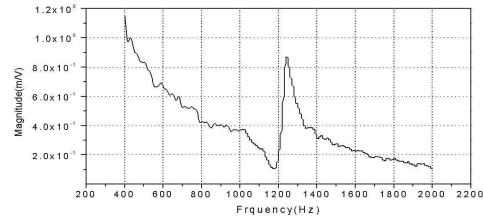
6. Conclusions

The angular electrostatic microactuator using skewed electrodes array (SEA) scheme was proposed. It was shown that SEA has better linearity than a parallel-plate type actuator and stronger force than a comb-drive type actuator. The moving and fixed electrodes are arranged to make the driving force perpendicular to the rotating moment of arm. By changing the electrode overlap length, the magnitude of electrostatic force and stable displacement will be changed. In order to optimize the design, electrostatic FE analysis were carried out and the empirical force model was established for SEA. Simulation was performed to make the comparison between the conventional type and the SEA. The proposed SEA generates actuating torque 2 times greater than the comb-drive and stable actuator displacement 40% greater than the parallel plate. The angular electrostatic microactuator using skewed electrode actuators(SEA) scheme that can position the pico-slider over $\pm 0.5 \mu m$ stroke using under 20 volts for a 2 kHz fine-tracking servo was designed.

References

[1] L. S. Fan. H. H. Ottesen. T. C. Reiley and R. W. Wood, "Magnetic recording head positioning at very high track densities using a microactuator-based two-stage servo system", IEEE Transaction on Industrial Electronics, Vol. 42., No. 3, 1995, pp.222-233

[2] J. Y. Yen, K. Hallamasek, R. Horowitz, "Track-following controller design for a compound disk drive actuator", Journal of Dynamic Systems, Measurement, and Control, Vol. 112, Sept. 1990, pp.391-492

[3] T. Takaishi, T. Imamura, Y. Mizoshita, S. Hasegawa, T. Ueno, T. Yamada, "Microactuator control for disk drives", IEEE Transactions on Magnetics, Vol. 32, 1996, pp.1863-1866

[4] S. Koganezawa, K. Takahashi, Y. Mizoshita Y. Uematsu, T. Yamada, D. Hasegawa, and T. Ueno, "A flexural piggy-back milli-actuator for over 5 Gbit/in2 density magnetic recording", IEEE Transactions on Magnetics, Vol.32, 1996, pp.3908-3910

[5] Yimin Niu, Wei Guo, Guoxiao Guo, Eng Hong Ong, and Tony Huang, "Piezoelectrically actuated suspension for hard disk drives", J. Info. Storage Pro. Syst., Vol. 1, 1999, pp.321-327

[6] D. H. F. Harper, R. A. Callafon, R. E. Skelton, and F. E. Talke, "Piezoelectric stack-based microactuator for hard disk drives", J. Info. Storage Pro. Syst., Vol. 1, 1999, pp.329-332

[7] Wei Guo and Jamshid Bozorgi, "Dual-stage servo system with microactuated head gimbal assemblies", J. Info. Storage Pro. Syst., Vol. 2, 2000, pp.101-108

[8] S. Nakamura, K. Suzuki, M. Ataka, and H. Fujita, "An electrostatic micro actuator for a magnetic head tracking system of hard disk drives", Transducers '97, Jun. 1997, pp.1081-1084

[9] S. Nakamura, K. Suzuki, H. Fujita, T. Numazawa and H. Takada, "A one-body MEMS device composed of mutually insulated metallic parts", Proceedings of IEEE Int. Workshop on MEMS, 1998, pp.278-283

[10] S. Nakamura, and H. Fujita, "Application of micromachine technologies to hard disk drives", IEEE Transactions on Magnetics, Vol.34, No.2, March 1998, pp.477-479

[11] L. S. Fan, "Design fabrication of microactuators for high density data storage", IEEE Transactions on Magnetics, Vol. 32, No. 3, May 1996, pp.1855-1862

[12] D. A. Horeley, M. B. Cohn, A. S. Singh, R. Horowitz, and A. P. Pisano, " Design and fabrication of an angular microactuator for magnetic disk drives", Journal of MEMS, Vol. 7, No. 2, June 1998, pp.141-148

[13] T. Hirano, L. S. Fan, J. Q. Gao and W. Y. Lee, " MEMS milliactuator for hard-disk-drive tracking servo", Journal of MEMS, Vol. 7, No. 2, June 1998, pp.149-155